Thermoelectric and structural correlations in (Sr_{1−x−y}Ca_{x}Nd_{y})TiO_{3} perovskites

H. Somaily, S. Kolesnik, B. Dabrowski, and O. Chmaissem

Thermoelectric and Structural Correlations in (Sr$_{1-x-y}$Ca$_x$Nd$_y$)TiO$_3$ Perovskites

H. Somaily, S. Kolesnik, B. Dabrowski, O. Chmaissem

Physics Department, Northern Illinois University, DeKalb IL 60115

Abstract

Structural and thermoelectric properties are reported for a specially designed class of *A*-site substituted perovskite titanates, (Sr$_{1-x-y}$Ca$_x$Nd$_y$)TiO$_3$. Two series synthesized with various *A*-site Sr-rich or Ca-rich (Sr-poor) concentrations were investigated using high resolution neutron powder diffraction as a function of temperature and Nd doping. Each series was designed to have a nominally constant tolerance factor at room temperature. We determine the room temperature structures as tetragonal I*4/mcm* and orthorhombic P*bnm* for the Sr-rich and Ca-rich series, respectively. Three low temperature orthorhombic structures, P*bnm*, I*bmm* and P*bcm* were also observed for the Sr-rich series; whereas, the symmetry of the Ca-rich series remains unchanged throughout the full measured temperature range. Thermoelectric properties of (Sr$_{1-x-y}$Ca$_x$Nd$_y$)TiO$_3$ were investigated and correlated with the structural variables. We succeeded in achieving a relatively high figure of merit ZT=0.07 at ~400 K in the Sr-rich Sr$_{0.76}$Ca$_{0.16}$Nd$_{0.08}$TiO$_3$ composition which is comparable to that of the best n-type *TE* SrTi$_{0.80}$Nb$_{0.20}$O$_3$ oxide material reported to date. For a fixed tolerance factor, the Nd doping enhances the carrier density and effective mass at the expense of the Seebeck coefficient. Thermal conductivity greatly reduces upon Nd doping in the Ca-rich series. With an enhanced Seebeck coefficient at elevated temperatures and reduced thermal conductivity, we predict that Sr$_{0.76}$Ca$_{0.16}$Nd$_{0.08}$TiO$_3$ and similar compositions have the potential to become some of the best materials in their class of thermoelectric oxides.

Introduction

Responding to the rapidly increasing demand for alternative energy, thermoelectric (*TE*) materials provide one key avenue for tackling this multifaceted global challenge. As scientists have come to realize the unfortunate limitations of implementing conventional thermoelectric materials such as the Bi_2Te_3 semiconductor for mid to high temperature applications, the gear soon shifted towards exploring promising alternatives such as perovskite ABO_3 oxides[1] thanks to their relatively low cost production and oxygen-reinforced stability at high temperatures.

Optimizing *TE* properties of a material for commercial use is widely regarded as a twofold challenge; one which is concerned with creating materials with low thermal conductivity κ and a large Seebeck coefficient S, and another which deals with understanding and exploiting the complex interactions between the material's structural and physical properties which largely influence its thermoelectric behavior. Substituted strontium titanates have demonstrated a strong potential for *TE* applications owing to high effective mass and large Seebeck coefficients. We believe the importance of our work stems from what we hope to be a successful disentanglement of the structural and thermoelectric properties in n-type $SrTiO_3$-based perovskite materials to whom our *A*-site substituted $(Sr_{1-x-y}Ca_xNd_y)TiO_3$ system belongs.

Apart from silicon, $SrTiO_3$ is one of the most common substrates in the thin film industry while its ferroelectric $BaTiO_3$ and $Ba_{1-x}Sr_xTiO_3$ counterparts have been used to fine tune dielectric properties and improve their suitability for advanced spintronic applications. Additionally, a variety of isovalent and multivalent substitutions at either the Sr^{2+} or the $3d^0$ Ti^{4+} sites have been successfully accomplished leading to drastic structural modifications mediated by TiO_6 octahedral twists and tilts that give rise to luminescence [2] ferrorelectricity (FE), antiferroelectricity (AFE) [3-5], metal-insulating transitions (MIT) [6,7], and thermoelectric (*TE*) properties [8]. Ferroelectricity was successfully induced in $SrTiO_3$ by replacing [16]O by the heavier [18]O oxygen isotope [9] while doped and reduced $SrTiO_3$ were reported to exhibit superconducting properties at low temperatures [10-12]. All of these results clearly demonstrate the strong potential of substituted strontium titanates which will be the subject of this study.

While intensive investigations have been carried out on *A*-site binary solid solutions like $Sr_{1-x}Ca_xTiO_3$ (SCT) or $Ba_{1-x}Sr_xTiO_3$ (BST), studies of more elaborate ternary systems such as

$Sr_{1-x-y}Ca_xNd_yTiO_3$ are relatively scarce. Perhaps this limitation is due in part to the compounded complexity of the diverse structural distortions that have so far been identified for intermediate SCT compositions [13-26]. However, such an extensive range of possible distortion induced symmetries and properties makes our goal to synthesize and investigate Nd^{3+}-substituted $Sr_{1-x-y}Ca_xNd_yTiO_3$ materials even more attractive and compelling.

      In this work, the double substitution of small ions like Ca^{2+} and Nd^{3+} at the Sr^{2+} site is used to tune the A-site ionic size and achieve specific constant or variable charge concentrations. Two distinct $Sr_{1-x-y}Ca_xNd_yTiO_3$ series were designed and fabricated having nearly constant room temperature tolerance factor, $t \ (= \frac{[A-O]}{\sqrt{2}\,[B-O]})$ with nominal values of 0.997 and 0.993. This seemingly tiny difference in the tolerance factor has tremendous effects on the materials structure and final symmetry as will be demonstrated in the next paragraph and subsequent sections. The actual [A-O] and [B-O] bond lengths used in this work were extracted from the Rietveld structural refinements using high-resolution neutron powder diffraction (NPD).

      In order to investigate the thermoelectric and structural properties for each t-constant series, we varied the electron doping concentration with Nd substitution levels y = 0, 0.01, 0.03, 0.08, and 0.20, thus simultaneously increasing the $Ti^{(4-y)}/Ti^{4+}$ ionic ratio at the B-site (single-electron n-type filling of the π^* conduction band in TiO_3 arrays with $3d\ t_{2g}^1 e_g^0$). On the other hand, varying the temperature at a fixed doping level leads to significant changes in the tolerance factor and hence to possible phase transitions [27]. In our materials, we expect the tolerance factor to increase progressively with temperature, as found in the related orthorhombic $CaTiO_3$ perovskite [28] for example (see section S1 in the Supplemental Material [29]), leading to structures with higher symmetries similar to those identified as tetragonal I4/mcm and cubic $Pm\overline{3}m$ (when $t = 1$). It is clear that the strong dependence of the tolerance factor on temperature leads to significant variations in the structural parameters (*i.e.* bond angles <Ti–O–Ti> and bond lengths) which in turn, at fixed band filling, cause a significant change of the electronic bandwidth W (~ cos [(π- <Ti–O–Ti>) /2]) [30].

      Property-wise, both the electrical conductivity σ and the Seebeck coefficient S of our investigated materials depend on the electronic doping level n (band filling) [31]. An equally important factor for determining transport and thermoelectric properties of the materials is the strength of the interactions between neighboring Ti atoms mediated by oxygen. These B–O–B

interactions, which can be strong enough to change the electronic state from localized to itinerant in some materials [6], are measured by the bandwidth W and hence they are sensitive to the degree of <Ti-O-Ti> bond angle distortions. Additionally, significant variations in the [Ti-O] bond length could play an important role in influencing the *TE* or *MIT* properties [32].

In addition to their exotic structural properties, this study also aims to explore the thermoelectric potential of our substituted strontium titanates for meeting some of the rapidly increasing demand for alternative energy. The performance of a good *TE* material is gauged by its figure of merit $ZT (= S^2 \sigma T \kappa^{-1})$ [33], with *ZT* values equal to or greater than 1 being highly desirable for efficient energy conversion. S, σ and κ are the Seebeck coefficient, electrical and thermal conductivities respectively. The first two parameters trend inversely due to their opposite dependence on the carrier density [34,35] thus making the optimization of *ZT* inherently difficult. Despite being good *TE* materials at room temperature, semiconducting Bi_2Te_3, PbTe, and $Si_{1-x}Ge_x$ alloys with high mobility μ [34,36] are examples of conventional thermoelectric materials that become unstable at higher temperatures [36]. Thus, materials with built-in oxygen like transition-metal-oxides emerge as promising alternatives for the capturing and recycling of wasted heat from automobile exhausts and industrial plants, *i.e.* for mid-to-high temperature applications [33].

P-type cobalt-based $NaCo_2O_4$ single crystals have been reported to possess power factor PF $(= S^2 \sigma)$ larger than that of Bi_2Te_3 [37,38] with *ZT*~1 at 800 K [34] while $Ca_3Co_4O_9$ exhibits *ZT*~ 0.30-0.40 at 1000 K [38,39]. On the other hand, n-type *TE* perovskites such as $ATiO_3$ and $AMnO_3$ remain under intensive investigations to optimize their performance as well. The $CaMnO_3$ compound exhibits a modest *TE* performance upon *A*-site (*B*-site) doping with Pr (W) with a maximum *ZT* of about 0.16 at 873K [40] (0.01 at 300K [41]), while the multiple site doping composition $Ca_{0.9}Y_{0.1}Mn_{1-x}Fe_xO_3$ gives *ZT*~0.02 at 400 K for x = 0.05 [42]. The *TE* performance of $SrTiO_3$-based ceramics far exceeds that of their manganite-based counterparts owing to the large Seebeck coefficient they exhibit because of their large carrier effective mass m* which is typically in the range of 6 to 10 m_o [39,43].

The enhanced effective mass (and hence S) [8] in electron-doped $SrTiO_3$ is the result of orbital degeneracy or equivalently the entropy per carrier. To the best of our knowledge, the highest *ZT* value reported [8] is for 20% *B*-site Nb-doped $SrTiO_3$ (*ZT*~0.37 at 1000 K) with a

power factor PF = 1.3 mW/mK^2. On the other hand, La-doped $Sr_{1-x}La_xTiO_3$ [44] exhibits a PF nearly three times larger (3.6 mW/mK^2); a value comparable to that of Bi_2Te_3 (4 mW/mK^2) [37]. In these materials, the La content was kept to a minimum (x = 0.1) just enough to enhance the n-type band filling while preserving the cubic $Pm\overline{3}m$ symmetry necessary for optimal orbital degeneracy.

The interesting *TE* capabilities displayed by these materials are mainly attributed to the orbital degeneracy of the Ti *3d* orbitals (triply degenerate t_{2g} comprising the conduction band) [44]. These results demonstrate the importance of optimizing the orbital degeneracy by keeping the octahedral distortions small (large *t* factor and larger <Ti–O–Ti> bond angles). Indeed, further splitting of the t_{2g} orbitals (lifting the degeneracy) into a doubly-degenerate e$_g$ and a singly-degenerate lower a$_{1g}$ orbital was found to lead to deterioration of the effective mass values and S in layered $Ca_3Co_4O_9$ perovskites [38], and in Nb-doped $SrO(SrTiO_3)n$ (n = 1, 2) materials [45]. These undesirable distortion-induced effects on the effective mass were reversed in rare earth (*RE*)-doped samples by the gradual increase of the bond angle with increasing temperature leading to the successful restoration of the triply degenerate Ti *3d* t_{2g} orbitals [45]. In some cases, however, breaking the orbital degeneracy by octahedral distortion as in $LaCoO_3$ helps stabilize the low spin configurations of Co^{3+} and Co^{4+} and leads to large thermopower properties [46,47]. Structural distortion of MnO_6 in Sr-doped $LaMnO_3$ was found to lift the double degeneracy of the upper *e*$_g$ band and S changes its sign from negative to positive accordingly [48].

Finally, using reliable structural information obtained by neutron powder diffraction (NPD), this study is designed to pave the way for a solid understanding of the correlations between the structural parameters ([Ti–O], <Ti–O–Ti> and the tolerance factor *t*), transport (σ, n, m*, μ, and thermal conductivity κ) and thermoelectric (S, PF, and ZT) properties in this class of promising perovskite titanates. Additionally, our work will thoroughly address currently disputed structures and shed light on the aspects of phase transformations in perovskites that may occur as substituted trivalent atoms change the oxidation state of the *B*-site transition metal.

Experimental Details

Materials were successfully synthesized using conventional solid-state synthesis techniques. A total of ten samples were prepared forming two distinct series of the perovskite titanates $A\text{TiO}_3$ $(A = \text{Sr}_{1-x-y}\text{Ca}_x\text{Nd}_y)$, with the compositions in each series designed to exhibit a nominally constant magnitude of the tolerance factor. The first series is Sr-rich with Sr contents ranging between 73 and 80% while the second series is Ca-rich (Sr-poor) with Sr concentrations reduced to 50–57%. Both the series have the same Nd substitution levels (*i.e.*, charge doping) of 0, 1, 3, 8 and 20%.

Oxygen off stoichiometry in oxides considerably influences their transport and thermoelectric properties [25,49,50]. To ensure oxygen-stoichiometric materials, Nd-free samples were synthesized in air at temperatures up to 1450-1480 ^{o}C while Nd-containing samples were synthesized in a slightly reducing atmosphere 1-5% H_2/Ar at temperatures up to 1480°C. Sample purity and phase formation were determined using in-house x-ray diffraction data collected at room temperature on a Rigaku D/MAX Diffractometer. Transport and thermoelectric properties were measured in the temperature range 10-400 K using a Quantum Design Physical Property Measurement System (PPMS) equipped with a Thermal Transport Option. Synchrotron x-ray data were collected on beamline 11BMB at the Advanced Photon Source at Argonne National Laboratory. Neutron Powder diffraction data were collected at temperatures between 13 and 300 K on the high-resolution time-of-flight diffractometer POWGEN at the Spallation Neutron Source of Oak Ridge National Laboratory [51]. Data analysis was performed using the Rietveld technique as implemented in the GSAS/EXPGUI software suite [52,53]. The oxygen stoichiometry is determined in our materials via a direct measurement of the oxygen content by oxidization at temperatures up to 1250 ^{o}C which indicated from measuring the weight difference that the initial oxygen content was ~3.00 oxygen atom per formulae unit with an uncertainty of no more than $\pm$ 0.01. On the other hand, refining the oxygen site occupancies using neutron powder diffraction data demonstrates that the oxygen content is fully stoichiometric for all the samples; see Table S3 in the Supplemental Material for the refined values [29]. Additionally, monitoring the measured Seebeck coefficient of our samples (which is directly related to the carrier concentration and is exclusively dependent on the Ti^{3+} content) as will be discussed in the

thermoelectric section of this paper, reveals nearly identical Seebeck coefficient values for each pair of same Nd content samples from the two Ca-rich and Sr-rich series (i.e. similar carrier concentrations) and provides evidence for our success to maintain a well-controlled oxygen stoichiometry through consistent synthesis procedures.

Results and Discussions

A. Structural Symmetries, Modeling and Analyses

While the crystal structure of the end members of the binary solid solution $Sr_{1-x}Ca_xTiO_3$ is known to transform from cubic $Pm\overline{3}m$ to the tetragonal I4/*mcm* symmetry [54] with an additional low temperature orthorhombic phase transition for $CaTiO_3$ (x=1) [28,54], intermediate compositions have been intensively investigated in the past decade but remain controversial. While several groups[13-17] report an orthorhombic P*bnm* (P*nma*) symmetry for only the $0.60 < x \le 1.00$ Ca-rich members, others [14,15,23,55] extend this orthorhombic distortion range to also include the $0.40 \le x \le 0.60$ members of the series. With even lower Ca concentrations, reports in the literature [13,16,18,55] suggest the structure of the $0.06 \le x < 0.40$ compositions to have become tetragonal I4/*mcm*; however, other studies propose the orthorhombic I*bmm* symmetry for the compositional range $0.10 \le x < 0.35$ [15,19,22,23] and the formation of a superstructure with the Pbcm symmetry [14,15,19,20,22] for $0.30 \le x < 0.40$. For compositions with $x \le 0.06$, most papers confirm the structure of these slightly doped materials as cubic $Pm\overline{3}m$ [14,16]. Furthermore, several other crystal structures have also been suggested from electron diffraction studies. For example, Woodward and co-workers [17] have reported the existence of room temperature monoclinic distortions in the specific composition range $x > 0.2$ and $x < 0.6$ while Anwar and Lalla [25,26] argued that the structure is rather orthorhombic $P2_12_12$ in the range $0.20 \le x < 0.35$.

Ca-rich materials

Rietveld analyses performed on all the members of the Ca rich series show the common orthorhombic P*bnm* structure (3-tilt system $a^-a^-c^+$ using Glazer notations [56,57], see section S2 in the Supplemental Material for details [29]) at all temperatures between 15 and 300 K and for all the Nd contents y = 0, 0.01, 0.03, 0.08, 0.20. No evidence for any phase transition was

detected. As expected for a mixed tilt system, three distinct sets of superlattice reflections relative to the parent cubic $Pm\bar{3}m$ structure were observed in the neutron diffraction data. Fig. 1 shows portions of the patterns at room temperature for SCT50. The refined structural parameters are listed in Table 1. For completeness, previously proposed models such as orthorhombic [25,26] $P2_12_12$, Bmmb [16] (another setting of Cmcm: $a^0b^+c^-$), and monoclinic $P2_1/m$ ($a^-b^+c^-$) [17] were all thoroughly tested and ruled out because of their poor indexing of the diffraction peaks and the large residual agreement factors after the final refinement cycles. A summary of a few select test models are shown in the Supplemental Material [29].

Sr-rich materials

The structural properties of the Sr rich materials are more eventful. Room temperature modeling for the Nd-free $Sr_{0.73}Ca_{0.27}TiO_3$ (SCT27) and $Sr_{0.73}Ca_{0.26}Nd_{0.01}TiO_3$ (Nd01) compositions was successfully performed using a previously proposed tetragonal structure with the I4/mcm space group symmetry [58]. Excellent fits between the observed and calculated intensities were obtained. Table 2 lists the refined room temperature structural parameters for SCT27.

Among other space group symmetries that were examined, the proposed orthorhombic Pbnm space group was ruled out because it could not produce all the observed reflections. Out-of-phase double tilt orthorhombic Ibmm ($a^-a^-c^0$) [14,15,22,24] and rhombohedral $R\bar{3}c$ ($a^-a^-a^-$) were also tested and rejected. The first gave a relatively large goodness of fit χ^2 value and it could not produce the expected tilts about the c-axis. The latter was unable to index many of the observed peaks, especially the main strong reflection at 2.25 Å. Additionally, the initially-singlet peaks of the $(h00)_p$ type associated with the cubic $Pm\bar{3}m$ phase should remain unchanged when the transition to the rhombohedral phase takes place whereas peaks of the type $(hhh)_p$ should split. Fig. 2 demonstrates a completely different behavior. Using similar arguments, $P2_12_12$ and $P2_1/m$ were examined and ruled out as well (see the Supplemental Material for details [29]). Thus, our results confirm that I4/mcm is the appropriate symmetry for our Sr-rich compositions at room temperature.

The I4/mcm phase remains stable as a function of decreasing temperature until a new set of weak superlattice reflections appear below 200 K that cannot be accounted for based on Glazer's 23 tilt systems, see Fig. 3 for example. Considering other possible sublattices led to the

doubling of the unit cell along the *c*-axis $[001]_p$ direction with the symmetry lowered to orthorhombic P*bcm* [14,20]. In this space group, the positive Ti ions move off-center in their original octahedral sites to result in displacive distortions thus making this phase ferroelectric. On the verge of the I4/*mcm*→P*bcm* phase transition at ~200 K, mixed-phase Rietveld refinements for $Sr_{0.73}Ca_{0.27}TiO_3$ successfully converged with phase weight fractions of 60% and 40%, respectively. Evidence for this mixed phase region is displayed in Fig. 4 showing the temperature evolution of the tetragonal reflection set $[440/008]_{I4/mcm}$ which is related to the singlet $[400]_{Pm-3m}$ cubic peak and is often examined to identify similar phase transitions. Between 150 and 200 K, the 440 and 008 peaks greatly overlap as the structure becomes orthorhombic.

The tetragonal I4/*mcm* stability range for $Sr_{0.74}Ca_{0.23}Nd_{0.03}TiO_3$ is wider (300 – 150 K) in comparison with the two previous Nd-free and Nd01 samples. A structural transition is also seen in a narrow temperature range close to ~125 K but to the common orthorhombic space group P*bnm*. Unlike the larger orthorhombic P*bcm* superstructure, the Ti cations in the P*bnm* space-group symmetry remain at the center of the severely distorted oxygen octahedra. As the Nd substitution increases to 8% ($Sr_{0.76}Ca_{0.16}Nd_{0.08}TiO_3$), an enhanced stability of the I4/*mcm* phase is achieved down to the lowest measured temperature of 13 K.

The last sample in the Sr-rich series is the Ca-free heavily doped $Sr_{0.80}Nd_{0.20}TiO_3$ material (Nd20). The structure is single phase tetragonal I4/*mcm* only in a narrow temperature range close to room temperature (300-275 K). However, broader peak profiles, observed below 275K, are indicative of extra anti-phase tilts about the *a* or *b* axes in addition to the existing rotation about the *c*-axis. The only candidate that satisfies this change is the orthorhombic I*bmm* ($a^- a^- c^0$) according to Glazer's tilt models.

Using only the I4/*mcm* space group in our refinements leads to significant mismatch between the observed and calculated profiles with a goodness of fit $\chi^2 =12.77$ while I*bmm* alone yields $\chi^2=11.35$. Therefore, the structure was refined successfully on the basis of a two-phase mixture of I4/*mcm* and I*bmm* which resulted in an excellent fit to the data and drastically lowered χ^2 to 4.35. Both phases coexist in the temperature range 275-15 K with I*bmm* rapidly becoming the majority phase.

B. Compositional (y)/Thermal Effects on the Lattice Parameters of Sr$_{(1-x-y)}$Ca$_{(x)}$Nd$_{(y)}$TiO$_3$

The lattice constants of our samples expand with increasing Nd^{3+} doping levels mainly due to the increased ionic ratio of Ti^{3+}/Ti^{4+}. The *c*-parameter of the I4/*mcm* phase appears to be expanding linearly in the measured temperature range. The I4/*mcm*–P*bnm* and I4/*mcm*–P*bcm* first-order structural transitions in some of our Sr-rich materials is manifest by the abrupt jumps in the *c*-(downwards) and *b*- lattice parameters (upwards) shown in Fig. 5(a,c). Curiously, the opposite behaviors of these parameters perfectly compensate to produce a continuous expansion of the unit cell volume upon increasing the temperature, see Fig 6.

In an earlier work, Ubic [59] proposed an empirical formula $a_{calc} = 0.06741 + 0.49052(r_A + r_O) + 1.29212 (r_B + r_O)$ as a function of Shannon's tabulated ionic radii [60] for the prediction of pseudocubic lattice constants of the diverse known perovskites ($a_p \approx b_p \approx c_p$). When compared with the lattice parameters measured for a large number of perovskite materials, the results of this formula were found to yield highly reliable values with an average relative error of no more than 0.60%. For our samples, we find that the best fit between the calculated (applying Ubic's formula) and measured room temperature lattice parameters is achieved when considering 8-fold coordinated *A*-cations in both the Sr- and Ca-rich series with relative errors of 0.84% and 0.80%, respectively (assuming 12-fold coordination would raise the error to 1.5% or more).

The apparent inadequacy of Shannon's ionic radii to help predicting the pseudocubic lattice constants using 12-fold coordinated *A*-site ionic sizes may be due to a host of different reasons including insufficient accuracy or simply to the fact that four of the twelve ligands in the distorted structures are usually long enough that they do not effectively contribute to ionic bonding. This is a well-known problem that has been repeatedly observed and invoked when explaining for example the magnetic properties of the colossal magnetoresistive perovskite manganites in terms of their internal structural parameters [27].

The effects of both the Nd content and temperature on the unit cell volume for all the investigated materials are depicted in Fig. 6. The unit cell volume of the parent SrTiO$_3$ [13,61-63] and CaTiO$_3$ [28,54,64] materials are shown for comparison.

C. Octahedral Tilts and Bond-Length Trends with Doping and Thermal Variations

Adjusting to the structural deformation in the form of A-O and B-O bond length mismatch ($t < 1$), the TiO_6 octahedra rotate cooperatively (Pbnm and I4/mcm structure) [6] about the c-axis to distort the equatorial Ti–O2–Ti bond angle from its ideal value of 180° in the cubic symmetry, and tilt relative to the (001) plane making the apical Ti–O1–Ti bond-angle less than 180° (Pbnm) [65]. Therefore, the average distortion of the <Ti–O–Ti> bond angle provides a direct measure of the overall structural deformation through its proportionality to the tolerance factor, $t \sim \cos^2(<\text{Ti-O-Ti}>)$ [27].

The magnitude of the tolerance factor t, which acts as the driving mechanism for the octahedral tilts, is kept nearly the same as that of the Nd-free sample of each series. Therefore, the <Ti–O–Ti> bond-angle is expected to reflect this doping-independency. Indeed, insignificant differences were observed between the Nd-free $Sr_{0.73}Ca_{0.27}TiO_3$ (174.54°) and the heavily doped $Sr_{0.80}Nd_{0.20}TiO_3$ (174.83°) samples of the Sr-rich series. Likewise, in the Ca-rich series the <Ti-O-Ti> bond angle ranges between 164.49° for Nd-free SCT50 and 165.96° for $Sr_{0.57}Ca_{0.23}Nd_{0.20}TiO_3$, see inset of top panel in Fig.7.

The effects of temperature on the <Ti–O–Ti> bond angle are more significant with first order phase transitions observed in the Sr-rich series. For example, a 5-6° change is determined for the y = 0, 1, and 3% samples between 300 and 15 K while the single-phase Nd8% sample has its <Ti–O–Ti> bond angle contracting by only ~0.7° over a similar temperature range. On the other hand, the temperature-dependence of the <Ti–O–Ti> bond angle is weaker and more uniform in the Ca-rich series in which phase transitions are absent with changes of only ~1.3° observed for all the members of this series as displayed in the bottom panel of Fig. 7. Based on these results, we conclude that larger effects of the bond angle should be expected on the physical properties of the Sr-rich compounds in agreement with their thermoelectric properties presented later.

Twelve A-O bond lengths of the A-site polyhedron exhibit a room temperature length distribution ranging from 2.62389(4) to 2.89176(2) Å and from 2.4862(32) to 3.0346(22) Å for the tetragonal Sr-rich and the more distorted orthorhombic Ca-rich series, respectively. Geometric averaging of the bonds reveals that the A-O bond-length average expands slightly as a function of increased Nd content (Table S3) or temperature (Figs. 5 (e and f)) with nearly

identical thermal expansion rates of 0.49% or 0.52% for the Sr-rich and Ca-rich series, respectively.

On the other hand, the geometrically averaged <Ti–O> bond lengths also elongate in both series upon increased substitution of the trivalent Nd^{3+} ions at the bivalent Sr^{2+}/Ca^{2+} sites. The lengthening of the bonds can be easily explained by the expected partial conversion, via Nd doping, of some Ti^{4+} ions into Ti^{3+} and the consequent formation of larger $[Ti^{3+}– O]$ bonds. The <Ti–O> bond length in the I*4/mcm* Sr-rich samples increases by 0.45% from 1.95028(9) (for Nd-free sample) while the P*bnm* members of the Ca-rich series exhibit a somewhat weaker response with the <Ti–O> bond length increasing by only 0.33% from its initial value of 1.9535(39) in the Nd-free $Sr_{0.50}Ca_{0.50}TiO_3$. It is worth noting that the structural sensitivity of the TiO_6 octahedra, quantified by the percent change in [Ti–O] bond length upon doping, appears to depend on the initial degree of structural distortions of the Nd-free parent compound. This observation should be taken into consideration when designing newer materials with specific desired tolerance factors.

Thanks to the unique choice of our carefully selected *A*-site cationic compositions, similar room temperature expansion rates are obtained as a function of Nd doping for the averaged <*A*–O> and √2 [Ti–O] bonds and hence the tolerance factor remains constant as intended for each series.

Finally, the combination of multiple compositions with various degrees of Sr, Ca and Nd contents at the disordered A-site and the high-resolution NPD data allow us to disentangle the average *A*-site to oxygen distances and to determine the individual Sr-O, Ca-O, Nd-O, Ti^{3+}-O and Ti^{4+} -O bond lengths. Values are summarized in Table 3 together with related values extracted from the literature [7,28,55,65-67].

D. Effects of Nd Substitution/Temperature on the Tolerance Factor

As shown in the previous section, the essentially constant room temperature tolerance factors upon increased Nd doping range between 0.9969(8) [Nd-free sample] and 0.9979(7) [Nd 20%] and 0.9909(9) [Nd-free] and 0.9927(4) for the Sr-rich and the orthorhombic Ca-rich series, respectively. Phase transition temperatures Ts both measured (from our NPD structural refinement results in the temperature range 13-300K) and calculated (by extrapolating and

fitting the *t* factor above room temperature to a power law in T in the form $t(T) = t_{0(T=0)} + AT^n$, with n=2 as shown in Fig. 8 and 9) are summarized in Table 4 and compared to the values acquired from synchrotron x-ray data and to the available literature data [13,28,61,68]. This method of estimation of the cubic $t(x,T) \geq 1$ to non-cubic $t(x,T) < 1$ structural transition with decreasing temperature is highly reliable because it does not depend on phases/symmetries below Ts. Moreover, the T^2 dependence of the tolerance factor on temperature is well known and has been observed for many other perovskite systems [27].

Two of the materials studied here have been intensively investigated in the literature, namely *Sr₀.₇₃Ca₀.₂₇TiO₃* and *Sr₀.₅₀Ca₀.₅₀TiO₃* for which our structural transitions sequence are in agreement [7,13,14,28]. On the other hand, claims [7] of a room temperature cubic structure for *Sr₀.₈₀Nd₀.₂₀TiO₃* are not sustained in this study.

E. Thermoelectric Properties of *Sr₁₋ₓ₋ᵧCaₓNdᵧTiO₃* Materials

Low thermal conductivity is required for the successful development of materials suitable for *TE* applications [27]. For example, thermoelectric effectiveness has been repeatedly confirmed to be limited by the phonons thermal conductivity in n-type $SrTiO_3$ oxides [8,34,44]. Due to strong electronic correlations, the thermal conductivity κ of our materials is dominated by a large energy gap and pronounced phononic lattice vibrations [69] so that the bipolar thermal conduction is negligible. The presence of three light oxygen anions per primitive unit cell presents quite a challenge in reducing κ due to their high phonon frequencies. In $SrTiO_3$-based materials, many methods have been used for reducing κ such as in the introduction of large lattice distortions by doping with smaller *RE* ions like Dy and Y [70], superlattice engineering with effective phonon scattering interfaces [45], and doping with heavy elements [35,36]. Here, we successfully reduced κ by partially suppressing the phonons with heavy *A*-site Nd doping (the atomic weight of Nd is larger than Ca and Sr combined) as shown in Fig.10 from the room temperature value of about 12 W/mK in Nb-doped $SrTiO_3$ [8,34] to as low as 1.5 W/mK in some samples. It is interesting to note that the linear proportionality of the *A*-site atomic weight on thermal conductivity is particularly emphasized in the Ca-rich series. For instance, the κ value of two samples with comparable *A*-site atomic weights such as the Sr-rich $Sr_{0.73}Ca_{0.26}Nd_{0.01}TiO_3$ and the Ca-rich $Sr_{0.53}Ca_{0.39}Nd_{0.08}TiO_3$ is reduced in the latter to nearly half its value in the Sr-

rich sample, which can be understood by taking into account the different degrees of distortions in the two materials. This experimental observation validate the concept that crystal structures can be tailored to exhibit low thermal conductivity [36,71]. The electronic contribution to thermal conductivity κ_e is estimated according to Wiedemann-Franz law [35] $\kappa_e = LT/\rho$. The value of Lorenz number L is obtained as a function of temperature from the absolute value of the measured Seebeck coefficient in μV/K as L (in WΩK^{-2}) = 1.5 + exp [- |S| /116] [72]. The electronic thermal conductivity was found to be negligibly small accounting for less than 1.5% of the total thermal conductivity in our materials and therefore we conclude that heat is predominantly conducted by the lattice (phonons). Successful predictions of the measured lattice thermal conductivity using Callaway and von Baeyer model [73,74] requires a necessary term that takes into account the phonon scattering via point defects. Point defects in our stoichiometric materials are introduced through a unique combination of A-site cations resulting in large mass fluctuations that effectively scatter the phonons. Disregarding such term would raise the discrepancy between calculated and measured thermal conductivity values to one order of magnitude. Thus, the observed reduction in thermal conductivity in our samples is due to the expected phonon-phonon interactions as well as point defect scattering mechanisms. More analytical details will be published elsewhere.

Unlike the electronic conductivity which can be affected by growth conditions, the (thermopower) Seebeck coefficient (S) is an intrinsic property of the material that depends fundamentally on the carrier concentration n [75] and on the effective mass m* [76,77]. For a *TE* semiconductor, S is typically a few hundred microvolts per Kelvin [36,37]. The monotonic linear Seebeck coefficient above 200 K show that S for both of our series follows the Mott model for thermopower in metals [36,78]. Thus, the slopes of the S(T) lines in Fig. 10 can be used to estimate the effective mass of Ti t_{2g} conduction band electrons at each Nd doping level according to the expression [44] S = [($8\pi^{8/3}$ k_B^2 m* $n^{-2/3}$)/($3^{5/3}$ h^2e)](r + 1)T, with m*, n, and r being the effective mass of electrons, the nominal carrier density (= y/ cell volume) and the scattering factor, respectively. In this work, we set the scattering factor r = 0.5 which is suitable for measurements at temperatures below 700 K [8,76]. The insets of Fig. 11 demonstrate that the incorporation of Nd ions into the lattice leads to a pronounced decrease in the Seebeck coefficient mainly due to the increased carrier concentration (n) as shown in the above equation.

The room temperature correlation between the effective mass of conduction electrons and the carrier density is also explored in the inset of Fig. 11 which shows the effective mass m* readily increasing with Nd content [34]. The theoretical prediction [76] of an inverse relationship between m* and n is therefore not sustained; however, our results are rather consistent with the experimental work reported for La and Nb-doped $SrTiO_3$ [8,44]. While the effective mass m* of pure $SrTiO_3$ is relatively high (~ 6-10 m_0) [43,79], it is reported that m* values for *B*-site doped bulk materials can be smaller. For instance, a density-of-states effective mass of 1.9 m_0 for m* is obtained for polycrystalline Nb 5%-$SrTiO_3$ [80]. Okuda and coworkers [44] estimated the effective mass of $SrTiO_3$ and 5% La-doped single crystal to be 1.17 and 1.62 m_0, respectively. The range of m* of our samples is 0.6-1.6 and 0.8-2.4 for the Sr-rich and Ca-rich series, respectively, in good agreement with the literature values.

In both series, m* and the Seebeck coefficient can be fitted with a natural logarithmic function in Nd content (y). On the other hand, the effective mass m* is reduced as the orbital overlap increases with increasing the bond angle <Ti–O–Ti>. At room temperature, the change in <Ti–O-Ti> is vanishingly small and hence the enhancement in m* with (y) is correlated with either the boosted [Ti–O] bond length [8,76,77] or more noticeably with the increase in carrier density in the conduction band [81].

Some of our materials exhibit room temperature |S| value close to 400 µV/K which is nearly four times that observed in both p-type $NaCo_2O_4$ [37] and $SrTi_{0.80}Nb_{0.20}O_3$ [77] and twice the value obtained with Bi_2Te_3 and other typical semiconductors [36]. We observe a strong correlation between the thermoelectric properties represented by the power factor PF (=$S^2\sigma$) and the structural tolerance factor for all the materials in the present study in the temperature range between 13 and 400 K as shown in Fig.11.

Seebeck coefficient for strongly correlated electron systems as the case in our materials is governed by the entropy of electronic states though the Heikes formula [75]. As T increases, spin and orbital degeneracies should lead to further enhancement of the measured S given for transition metal oxides [46,82] as: S= - [K_B/e] ln (g_{Ti}^{4+} /g_{Ti}^{3+} (1-y/y)) , where g is the orbital and spin degeneracy factor for electrons in Ti 3*d* orbitals for Ti^{4+} and Ti^{3+} ions, y is the doping concentration of Nd atoms. The resulting six-fold degeneracy (-[K_B/e] ln (6) = -154 µV/K) is optimal when the octahedral TiO_6 distortion is minimum (*t* factor =1).

Tuning the electrical conductivity σ of ceramic oxides is possible either by doping or by creating oxygen vacancies [41]. Our samples exhibit upon warming electrical resistivity behaviors typical of semiconductors ($d\rho/dT < 0$). In Sr-rich Nd8% sample, the measured resistivity (9.9 mΩ.cm) is significantly lower than that reported for polycrystalline $Ca_3Co_4O_9$ (15mΩ.cm) [38] but about one or two orders of magnitude larger than $NaCo_2O_4$ [37] and Bi_2Te_3 [36] single crystals which is still considered practically acceptable considering the polycrystalline nature of our materials. The temperature dependence of resistivity ρ is plotted in Fig.10. The measured resistivity ρ, exhibits strong correlations with the structural parameters; in particular with the average bond length <Ti–O> and the tilt angle for both series. For example, the samples with 8% Nd in the two series exhibit a five order of magnitude difference in the measured resistivity due to the dissimilarity in their crystal structure and a pronounced difference of about 10° in the <Ti–O–Ti> bond angle which influences the bandwidth W. In the lightly distorted Sr-rich series, resistivity is remarkably reduced with increasing Nd doping concentration up to y = 0.08. This enhancement in the conductivity σ is attributed to the increase in the electron concentration of the system ($\sigma = ne\mu$) [36]. In both series, the electrical conduction in the samples with low Nd doping levels (i.e. y = 0.01, 0.03, and 0.08) which exhibit non-metallic/semiconducting properties can be well explained on the basis of thermally activated conduction of impurity band formed exclusively from the Ti^{3+} 1-electron t_{2g} states in which the logarithmic resistivity of the materials varies linearly with inverse temperature following the Arrhenius law [83] similar to other n-type doped semiconductors [84]. On the other hand, the conductivity in heavily doped samples (y=0.20) is ascribed to the process of thermal activation of small polaron hopping which is found to coexist with variable range hopping mechanism (VRH) [85] as the temperature decreases. Full details of the resistivity analysis and properties will be presented elsewhere.

Finally, the highest figure of merit obtained in this study is for the 8% Nd-doped Sr-rich sample with a ZT value of ~ 0.07 at 400 K which is comparable to the value (ZT~0.08) reported for 20% Nb-doped $SrTiO_3$ that possesses to the best of our knowledge the highest *ZT* value reported so far for n-type oxides. Additionally, our materials offer important advantages like the measured thermal conductivity κ which is less than half that in Nb-doped $SrTiO_3$ (κ = 8 W/m.K) [34] and a Seebeck value ~140 µV/K for $Sr_{0.76}Ca_{0.16}Nd_{0.08}TiO_3$ which is significantly larger than

the 100 µV/K reported for $NaCo_2O_4$ single crystals known to exhibit the best *TE* capabilities among all the related oxide materials. Taking these factors into account, we predict that our Sr-rich $Sr_{0.76}Ca_{0.16}Nd_{0.08}TiO_3$ sample should possess a ZT value at higher temperatures, when transition to the higher cubic symmetry with optimal orbital degeneracy occurs, that could easily exceed 0.37 [8] and thus could emerge as a very promising n-type oxide material for thermoelectric applications.

Conclusions

In conclusion, two series of *A*-site doubly substituted $(Sr_{1-x}Ca_xNd_y)TiO_3$ materials have been successfully synthesized with various concentrations designed to exhibit two distinct nominally constant tolerance factor values at room temperature. The crystal structures of these materials have been characterized using high-resolution neutron powder diffraction as a function of temperature and Nd doping. At room temperature, the Sr-rich and Sr-poor series crystallize in the space group symmetries of tetragonal I*4/mcm* and orthorhombic P*bnm*, respectively, and remain so upon increasing the Nd^{3+} content. However, three different orthorhombic phases, P*bnm*, I*bmm*, P*bcm*, are determined for the Sr-rich series as a function of decreasing temperature; whereas, for the Sr-poor series the P*bnm* structure persists throughout the studied temperature range.

Variations of structural parameters such as lattice parameters and tolerance factor were successfully correlated to changes in octahedral tilt angles. Thermoelectric properties were also investigated. For fixed tolerance factor, we found that Nd doping enhances the carrier density and effective mass at the expense of the Seebeck coefficient. Both m* and S vary as logarithmic functions of the Nd doping level. Thermal conductivity κ was found to be quite sensitive to increased Nd doping in the Sr-rich series as it greatly reduces in response to subtle structural changes. We succeeded in achieving a high figure of merit ZT = 0.07 at 400 K in the Sr-rich composition $Sr_{0.76}Ca_{0.16}Nd_{0.08}TiO_3$ which is comparable to the best *TE* values reported so far for similar n-type oxide materials (*e.g.*, $SrTi_{0.80}Nb_{0.20}O_3$). With further enhancement of the Seebeck coefficient together with even more reduced thermal conductivity expected at higher temperatures, we predict that our $Sr_{0.76}Ca_{0.16}Nd_{0.08}TiO_3$ and similar compositions have the great

potential to become among the best known thermoelectric materials with practical *TE* capabilities.

Acknowledgements

References:

[1]   F. S. Galasso, *Structure, Properties and Preparation of Perovskite-Type Compounds: International Series of Monographs in Solid State Physics* (Elsevier, 2013), Vol. 5

[2]   D. Kan, R. Kanda, Y. Kanemitsu, Y. Shimakawa, M. Takano, T. Terashima, and A. Ishizumi, Appl. Phys. Lett. **88**, 1916 (2006).

[3]   R. E. Cohen, Nature **358**, 136 (1992).

[4]   J. G. Bednorz and K. A. Müller, Phys. Rev. Lett. **52**, 2289 (1984).

[5]   J. H. Haeni *et al.*, Nature **430**, 758 (2004).

[6]   S. L. Cooper, T. Egami, J. B. Goodenough, J. S. Zhou, and J. B. Goodenough, *Localized to itinerant electronic transition in perovskite oxides* (Springer, 2003), Vol. 98

[7]   C. Eylem, H. L. Ju, B. W. Eichhorn, and R. L. Greene, J. Solid State Chem. **114**, 164 (1995).

[8]   S. Ohta, T. Nomura, H. Ohta, M. Hirano, H. Hosono, and K. Koumoto, Appl. Phys. Lett. **87**, 092108 (2005).

[9]   M. Itoh, R. Wang, Y. Inaguma, T. Yamaguchi, Y.-J. Shan, and T. Nakamura, Phys. Rev. Lett. **82**, 3540 (1999).

[10]   J. Schooley, W. Hosler, E. Ambler, J. Becker, M. L. Cohen, and C. Koonce, Phys. Rev. Lett. **14**, 305 (1965).

[11]   J. F. Schooley, W. R. Hosler, and M. L. Cohen, Phys. Rev. Lett. **12**, 474 (1964).

[12]   G. Binnig, A. Baratoff, H. Hoenig, and J. Bednorz, Phys. Rev. Lett. **45**, 1352 (1980).

[13]   S. Qin, A. I. Becerro, F. Seifert, J. Gottsmann, and J. Jiang, J. Mater. Chem. **10**, 1609 (2000).

[14]   R. Ranjan, D. Pandey, W. Schuddinck, O. Richard, P. De Meulenaere, J. Van Landuyt, and G. Van Tendeloo, J. Solid State Chem. **162**, 20 (2001).

[15]   S. K. Mishra, R. Ranjan, D. Pandey, and H. T. Stokes, J. Phys. Condens. Matter **18**, 1885 (2006).

[16]   C. J. Ball, B. D. Begg, D. J. Cookson, G. J. Thorogood, and E. R. Vance, J. Solid State Chem. **139**, 238 (1998).

[17]   D. I. Woodward, P. L. Wise, W. E. Lee, and I. M. Reaney, J. Phys. Condens. Matter **18**, 2401 (2006).

[18]   C. J. Howard, R. L. Withers, Z. Zhang, K. Osaka, K. Kato, and M. Takata, J. Phys. Condens. Matter **17**, 459 (2005).

[19]   P. Ranson, R. Ouillon, J. P. Pinan‑Lucarre, P. Pruzan, S. K. Mishra, R. Ranjan, and D. Pandey, J. Raman Spectrosc. **36**, 898 (2005).

[20]   C. J. Howard, R. L. Withers, K. S. Knight, and Z. Zhang, J. Phys. Condens. Matter **20**, 135202 (2008).

[21]   B. J. Kennedy, C. J. Howard, and B. C. Chakoumakos, J. Phys. Condens. Matter **11**, 1479 (1999).

[22]   S. K. Mishra, R. Ranjan, D. Pandey, and B. J. Kennedy, J. Appl. Phys. **91**, 4447 (2002).

[23]   R. Ranjan, P. Dhananjai, V. Siruguri, P. S. R. Krishna, and S. K. Paranjpe, J. Phys. Condens. Matter **11**, 2233 (1999).

[24]   M. A. Carpenter, C. J. Howard, K. S. Knight, and Z. Zhang, J. Phys. Condens. Matter **18**, 10725 (2006).

[25]   S. Anwar and N. Lalla, Appl. Phys. Lett. **92**, 212901 (2008).

[26]   S. Anwar and N. Lalla, Solid State Sciences **10**, 307 (2008).
[27]   B. Dabrowski, O. Chmaissem, J. Mais, S. Kolesnik, J. D. Jorgensen, and S. Short, J. Solid State Chem. **170**, 154 (2003).
[28]   M. Yashima and R. Ali, Solid State Ionics **180**, 120 (2009).
[29]   See Supplemental Material at [URL] for Results of Glazer Notation, Test Models Analysis, and Tolerance Factor Variations with Temperature.
[30]   O. Chmaissem, B. Dabrowski, S. Kolesnik, J. Mais, L. Suescun, and J. D. Jorgensen, Phys. Rev. B **74**, 144415 (2006).
[31]   M. Imada, A. Fujimori, and Y. Tokura, Rev. Mod. Phys. **70**, 1039 (1998).
[32]   M. A. Subramanian and M. H. Whangbo, J. Solid State Chem. **96**, 461 (1992).
[33]   L. E. Bell, Science **321**, 1457 (2008).
[34]   H. J. Goldsmid, *Introduction to thermoelectricity* (Springer Science & Business Media, 2009), Vol. 121
[35]   Y. Pei, X. Shi, A. LaLonde, H. Wang, L. Chen, and G. J. Snyder, Nature **473**, 66 (2011).
[36]   C. C. Sorrell, J. Nowotny, and S. Sugihara, *Materials for energy conversion devices* (Elsevier, 2005).
[37]   I. Terasaki, Y. Sasago, and K. Uchinokura, Phys. Rev. B **56**, 12685 (1997).
[38]   Y. Miyazaki, Solid State Ionics **172**, 463 (2004).
[39]   H. Ohta, K. Sugiura, and K. Koumoto, Inorg. Chem. **47**, 8429 (2008).
[40]   F. Zhang, N. I. U. Baocheng, K. Zhang, X. Zhang, L. U. Qingmei, and J. Zhang, J. of Rare Earths **31**, 885 (2013).
[41]   R. Kabir, T. Zhang, D. Wang, R. Donelson, R. Tian, T. T. Tan, and S. Li, J. Mater. Sci. **49**, 7522 (2014).
[42]   L. T. Hung, N. Van Nong, L. Han, D. Le Minh, K. A. Borup, B. B. Iversen, N. Pryds, and S. Linderoth, J. Mater. Sci. **48**, 2817 (2013).
[43]   H. P. R. Frederikse, W. R. Thurber, and W. R. Hosler, Phys. Rev. **134**, A442 (1964).
[44]   T. Okuda, K. Nakanishi, S. Miyasaka, and Y. Tokura, Phys. Rev. B **63**, 113104 (2001).
[45]   Y. Wang, K. H. Lee, H. Ohta, and K. Koumoto, J. Appl. Phys. **105**, 103701 (2009).
[46]   W. Koshibae, K. Tsutsui, and S. Maekawa, Phys. Rev. B **62**, 6869 (2000).
[47]   S. Hébert, D. Flahaut, C. Martin, S. Lemonnier, J. Noudem, C. Goupil, A. Maignan, and J. Hejtmanek, Prog. Solid State Chem. **35**, 457 (2007).
[48]   A. Asamitsu, Y. Moritomo, and Y. Tokura, Phys. Rev. B **53**, R2952 (1996).
[49]   H. Muta, K. Kurosaki, and S. Yamanaka, J. Alloys Compd. **392**, 306 (2005).
[50]   T. Katsufuji, Y. Taguchi, and Y. Tokura, Phys. Rev. B **56**, 10145 (1997).
[51]   A. Huq, J. P. Hodges, O. Gourdon, and L. Heroux, Z. Kristallogr. Proc **1**, 127 (2011).
[52]   B. H. Toby, J. Appl. Crystallogr. **34**, 210 (2001).
[53]   A. C. Larson and R. B. Von Dreele, Los Alamos National Laboratory, New Mexico, USA, 86 (2000).
[54]   S. A. T. Redfern, J. Phys. Condens. Matter **8**, 8267 (1996).
[55]   T. Yamanaka, N. Hirai, and Y. Komatsu, Am. Mineral. **87**, 1183 (2002).
[56]   A. M. Glazer, Acta Crystallogr. Sec. B **28**, 3384 (1972).
[57]   A. M. Glazer, Acta Crystallogr. Sec. A **31**, 756 (1975).
[58]   E. Prince, A. J. C. Wilson, T. Hahn, and U. Shmueli, *International tables for crystallography* (International Union of Crystallography, 1999).
[59]   R. Ubic, J. Am. Ceram. Soc. **90**, 3326 (2007).

[60]   R. D. t. Shannon, Acta Crystallogr. Sec. A **32**, 751 (1976).
[61]   J. M. Kiat and T. Roisnel,J. Phys. Condens. Matter **8**, 3471 (1996).
[62]   Y. Kuroiwa, S. Aoyagi, A. Sawada, E. Nishibori, M. Takata, M. Sakata, H. Tanaka, and J. Harada, J. Korean Phys. Soc. **42**, 1425 (2003).
[63]   Y. A. Abramov, V. G. Tsirelson, V. E. Zavodnik, S. A. Ivanov, and I. D. Brown, Acta Crystallogr. Sec. B **51**, 942 (1995).
[64]   K. S. Knight, J. Alloys Compd. **509**, 6337 (2011).
[65]   A. C. Komarek, H. Roth, M. Cwik, W. D. Stein, J. Baier, M. Kriener, F. Bourée, T. Lorenz, and M. Braden, Phys. Rev. B **75**, 224402 (2007).
[66]   M. Cwik *et al.*, Phys. Rev. B **68**, 060401 (2003).
[67]   M. Eitel and J. E. Greedan, J. of the Less-Common Met. **116**, 95 (1986).
[68]   G. Shirane and Y. Yamada, Phys. Rev. **177**, 858 (1969).
[69]   J. Robertson, J. Vac. Sci. Technol. B **18**, 1785 (2000).
[70]   J. Liu, C. L. Wang, Y. Li, W. B. Su, Y. H. Zhu, J. C. Li, and L. M. Mei, J. Appl. Phys. **114**, 223714 (2013).
[71]   F. J. DiSalvo, Science **285**, 703 (1999).
[72]   H.-S. Kim, Z. M. Gibbs, Y. Tang, H. Wang, and G. J. Snyder, APL materials **3**, 041506 (2015).
[73]   J. Callaway, Phys. Rev. **113**, 1046 (1959).
[74]   J. Callaway and H. C. von Baeyer, Phys. Rev. **120**, 1149 (1960).
[75]   P. M. Chaikin and G. Beni, Phys. Rev. B **13**, 647 (1976).
[76]   W. Wunderlich, H. Ohta, and K. Koumoto, Phys. B **404**, 2202 (2009).
[77]   M. Yamamoto, H. Ohta, and K. Koumoto, Appl. Phys. Lett. **90**, 072101 (2007).
[78]   M. Jonson and G. D. Mahan, Phys. Rev. B **21**, 4223 (1980).
[79]   J. Ravichandran, W. Siemons, M. Scullin, S. Mukerjee, M. Huijben, J. Moore, A. Majumdar, and R. Ramesh, Phys. Rev. B **83**, 035101 (2011).
[80]   M. Ahrens, R. Merkle, B. Rahmati, and J. Maier, Phys. B **393**, 239 (2007).
[81]   C. B. Vining, J. Appl. Phys. **69**, 331 (1991).
[82]   D. B. Marsh and P. E. Parris, Phys. Rev. B **54**, 7720 (1996).
[83]   L. Zhang and Z.-J. Tang, Phys. Rev. B **70**, 174306 (2004).
[84]   N. Mott, J. Non-Cryst. Solids **1**, 1 (1968).
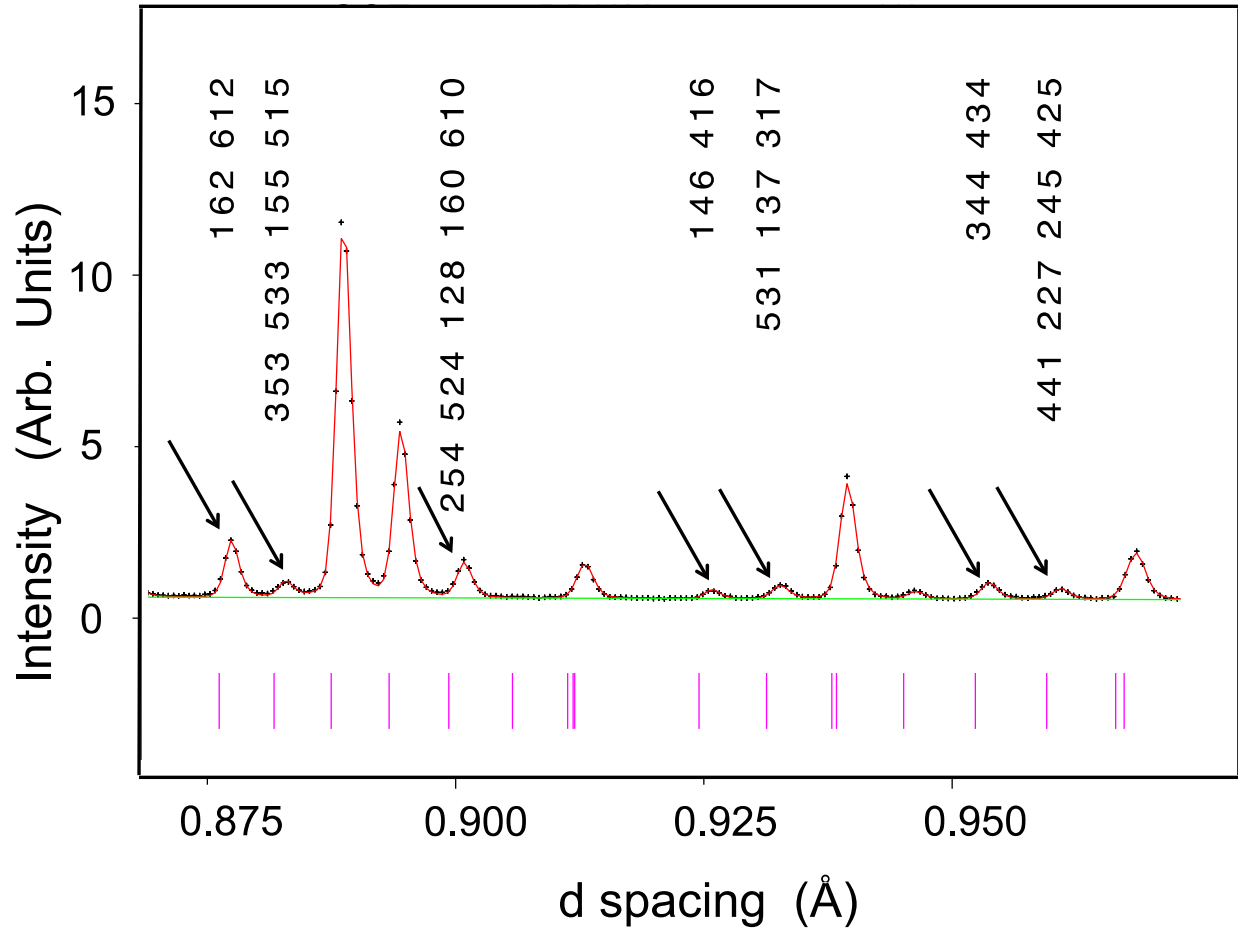[85]   N. Mott and E. Davis, *Electronic process in non-crystalline materials* (Oxford University Press, 1971).

Figure 1: (Color online) Room temperature diffraction data for SCT50 in a narrow d spacing range. Superlattice reflections marked by arrows indicate the orthorhombic P*bnm* (a⁻a⁻c⁺) symmetry. Tick marks represent symmetry allowed reflections. The [612 162] reflections of the (odd odd even) OOE type (labeling of reflections is with respect to the parent cubic subcell) are due to in-phase tilting, whereas the [533 353 515 155] index set as EEO are due to *A*-cation displacements in both the x and y directions. Marked peaks have no corresponding reflections in the I4/*mcm* tilt system. Strong peaks of the EEE type correspond to the elementary unit cell. Peaks of the OOO type are associated with anti-phase tilting.
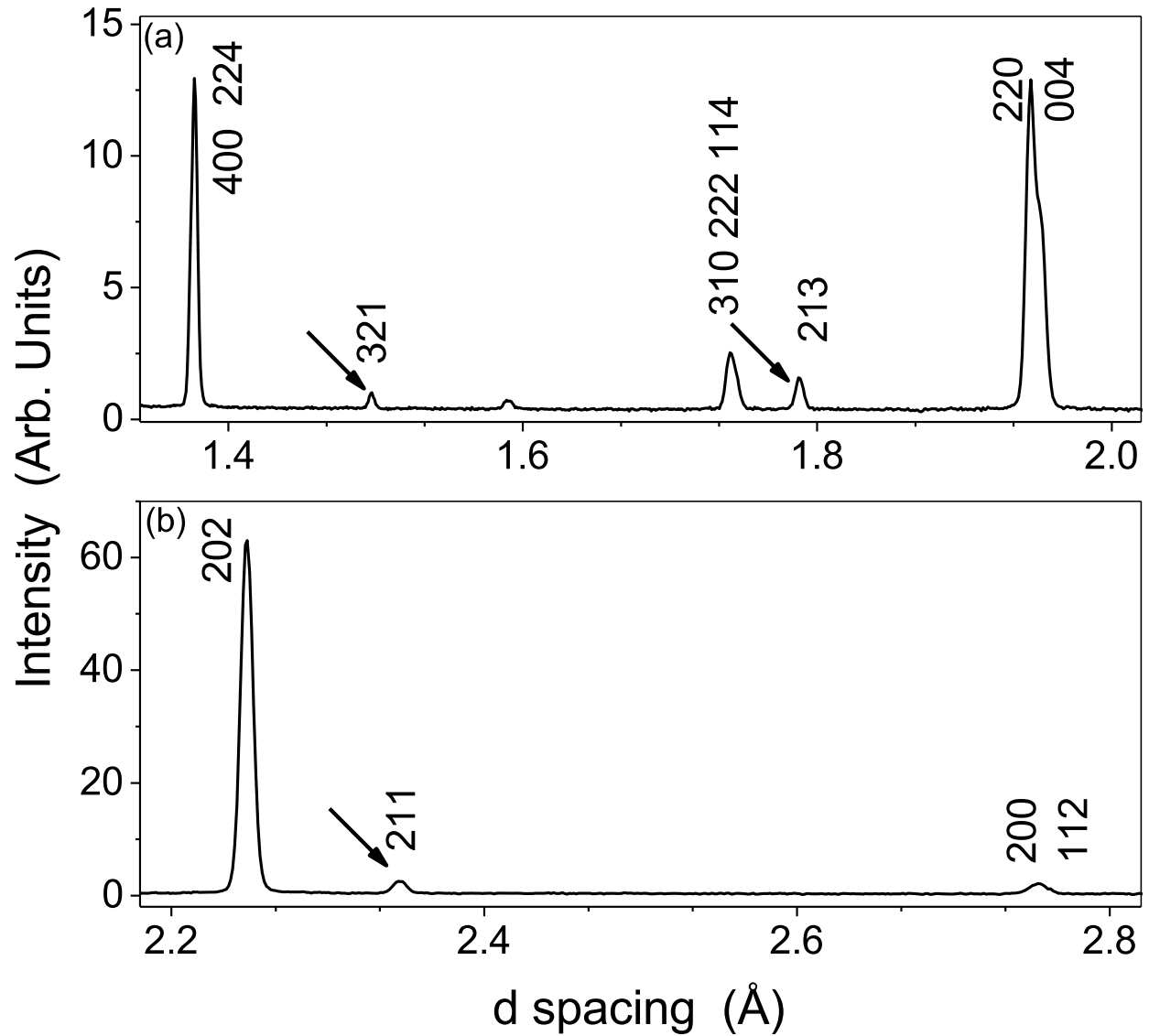
Figure 2: Extracts from room temperature neutron diffraction patterns for $Sr_{0.73}Ca_{0.27}TiO_3$. Superlattice reflections of the OOO type with respect to the parent cubic subcell are indicated by arrows in (a) and (b). The tetragonal structure is demonstrated by the splitting of the primitive cubic $(200)_p$ peak into a [220/004] doublet ($I4/mcm$ symmetry).
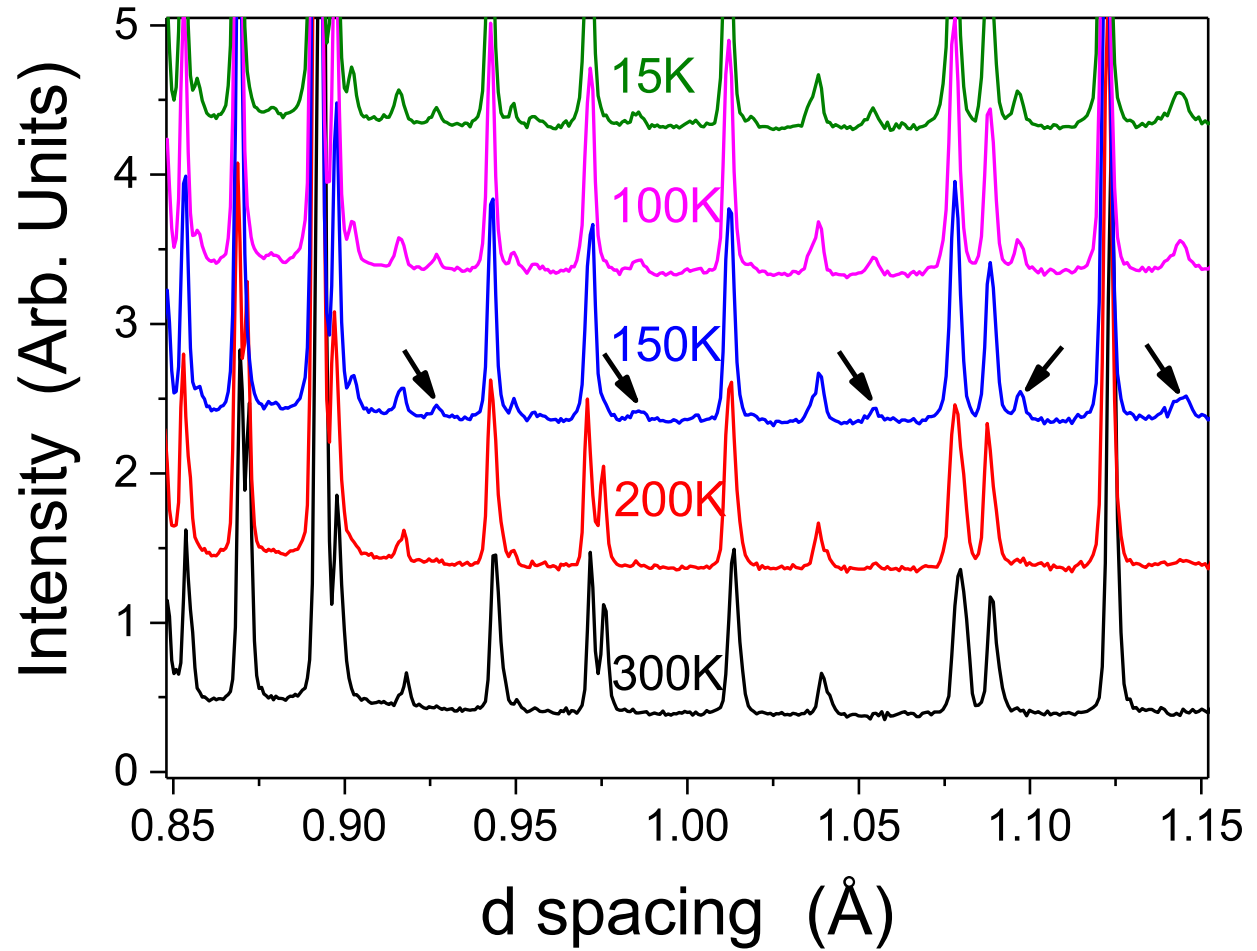
Figure 3: (Color online) Neutron diffraction patterns showing superlattice reflections for $Sr_{0.73}Ca_{0.26}Nd_{0.01}TiO_3$ at select temperatures. Weak peaks arise due to distortions from the 300 K tetragonal structures. Strong peaks appear truncated in the figure to emphasize the weak reflections.
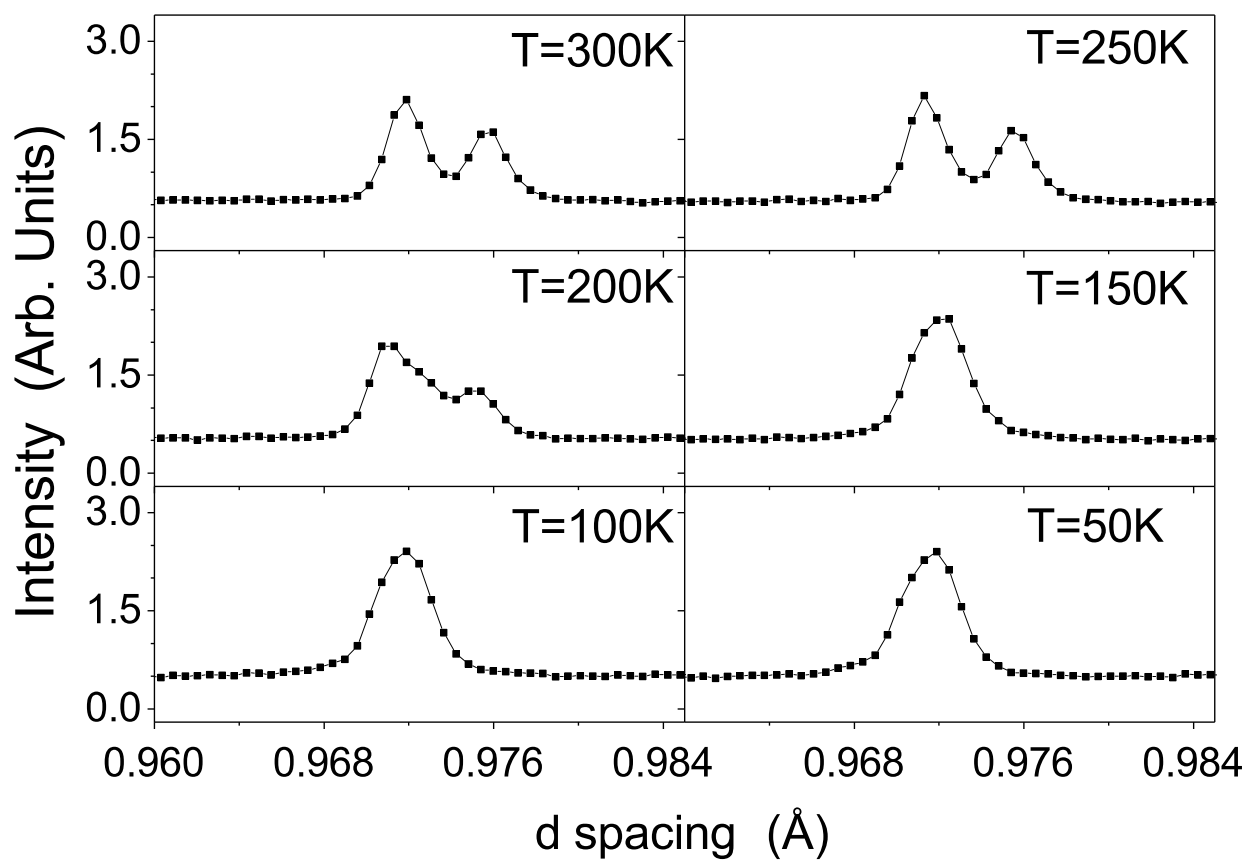
Figure 4: Temperature evolution of the tetragonal reflections $(440/008)_{I4/mcm}$ in SCT27 showing evidence of a mixed phase region between 150 and 200K.
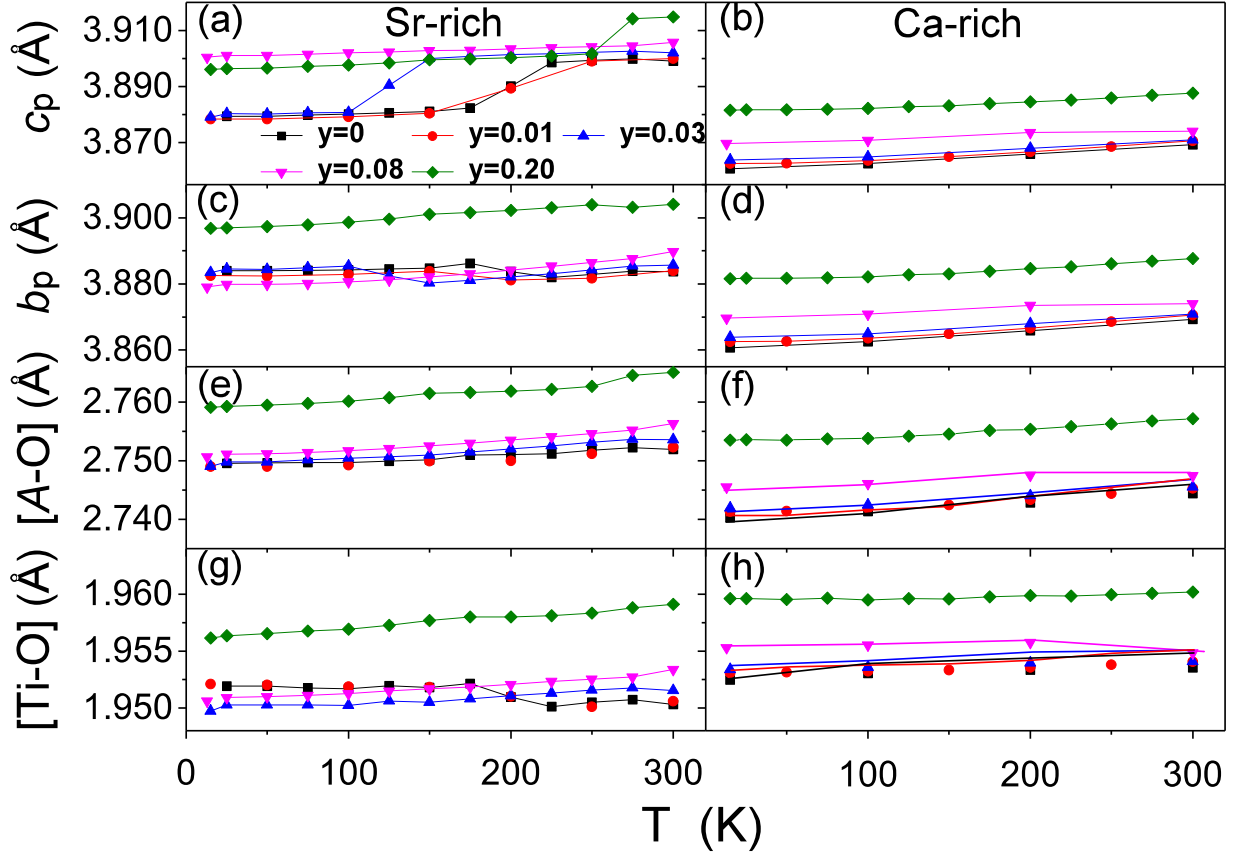
Figure 5: (Color online) Plots of reduced c ($c_p = c/2$) and b_p ($= b/\sqrt{2}$) lattice constants and the bond lenghts [A–O] and [Ti–O] as a function of temperature.
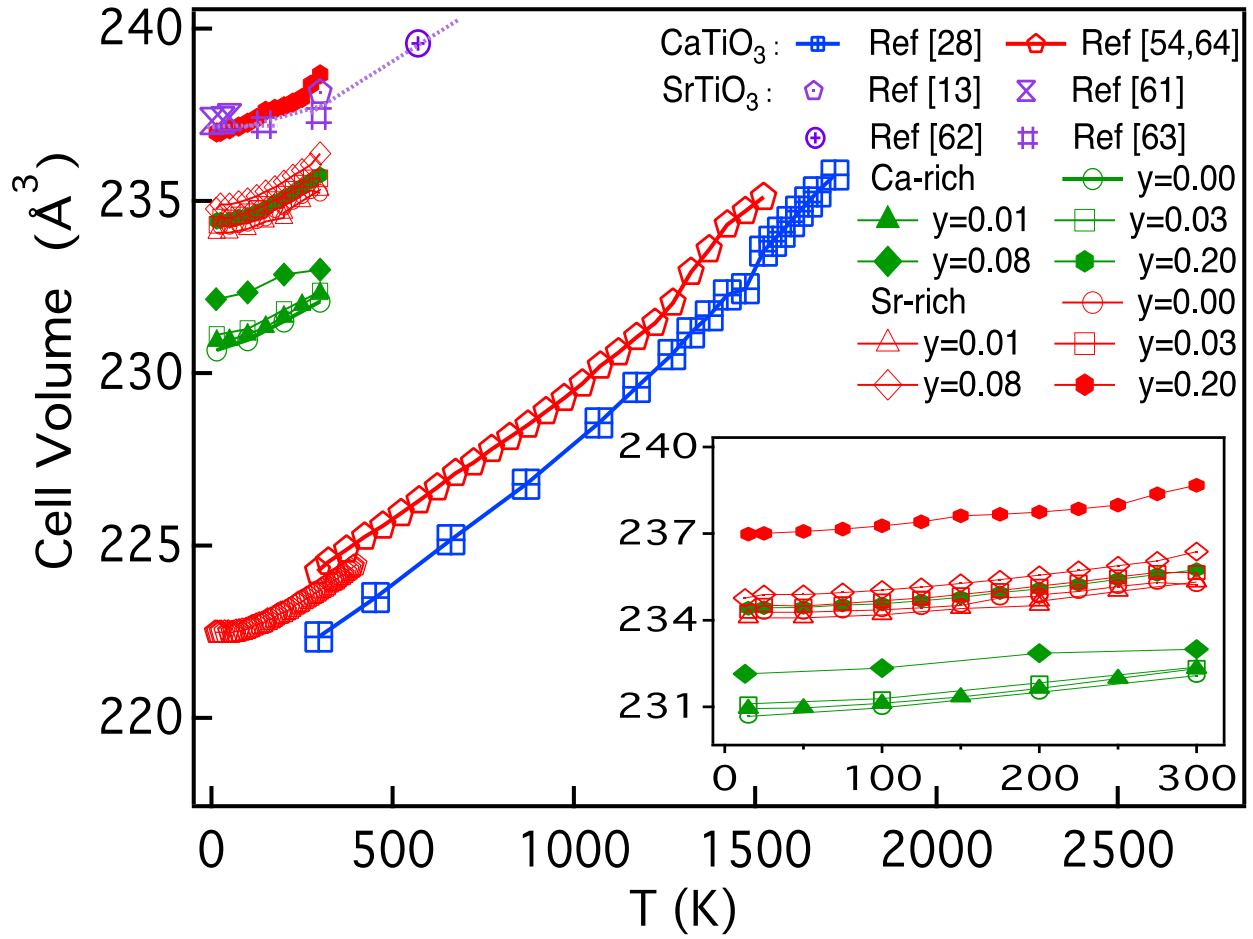
Figure 6: (Color online) Unit cell volume behavior as a function of temperature for all of our Sr-rich and Ca-rich samples together with those of the parent $CaTiO_3$ and $SrTiO_3$ materials as extracted from multiple literature references. The inset shows the zoomed in data for both series.
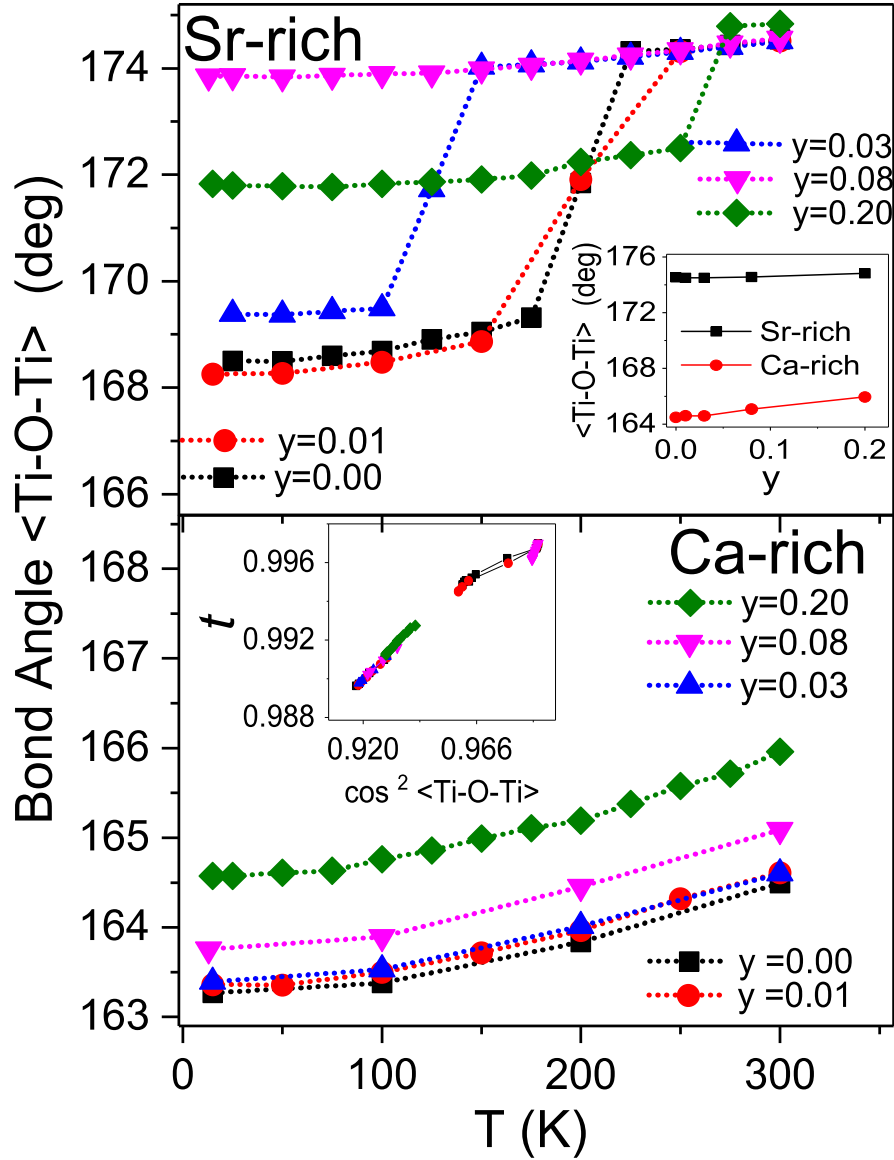
Figure 7: (Color online) Top: T-variations of the average <Ti–O-Ti> bond angle for Sr-rich materials. The abrupt drops correlate with first-order phase transitions to lower symmetries. The bond angles level-off at low temperatures while at higher temperature they tend to converge to a common value for all the samples in this series. The inset shows the <Ti–O-Ti> bond angle behavior at room temperature as a function of Nd substitutions which is nearly constant for each series in agreement with the designed *t*-constant requirement. Bottom: temperature-dependent <Ti–O-Ti> bond angle in the Ca-rich series. The TiO_6 octahedral distortion is gradually suppressed as a function of increasing temperature. The inset shows the linear relationship between tolerance factor (*t*) and the squared cosine of the bond angle.
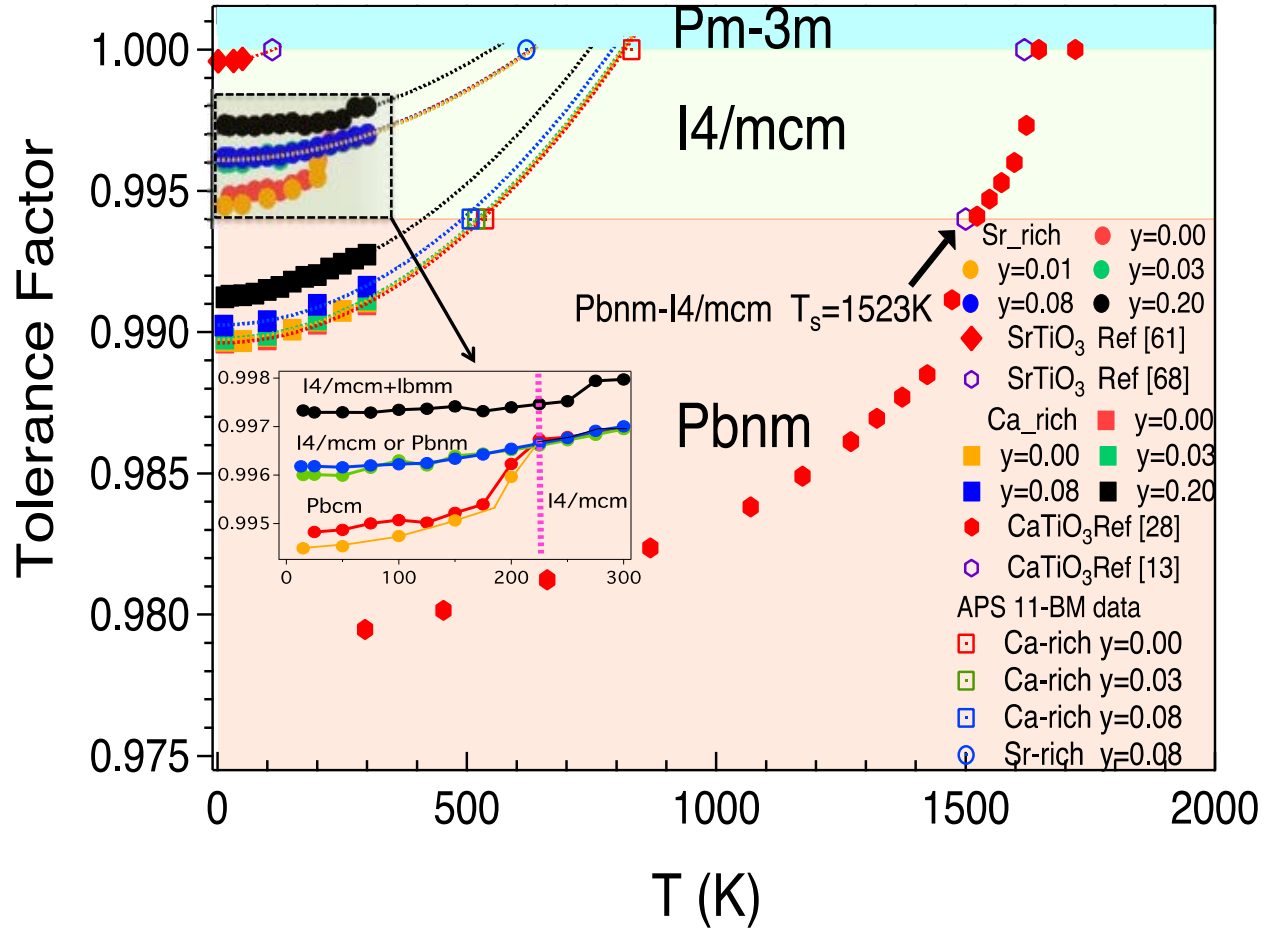
Figure 8: (Color online) Tolerance factor versus temperature for the full $Sr_{(1-x-y)}Ca_{(x)}Nd_{(y)}TiO_3$ system. Literature data are used for the parent $SrTiO_3$ [61] and $CaTiO_3$ [13,28] materials. For $SrTiO_3$, low temperature data [61] in the 1.5 to 50 K range were extrapolated to $t = 1$ using the same power law employed with the other materials from which we obtained a transition temperature, T_S, to the cubic symmetry at ~110 K in excellent agreement with the literature [68]. Solid lines correspond to the fitting of the NPD data (10-300K) to elevated temperatures. Open symbols shown on the critical cubic and tetragonal transition lines are data obtained experimentally from the APS 11BMB x-ray beamline for comparison. See Table 4 for a full summary of the transition temperatures. Inset shows the thermal variation of tolerance factor for the Sr-rich series where various low-T crystal structures were observed.
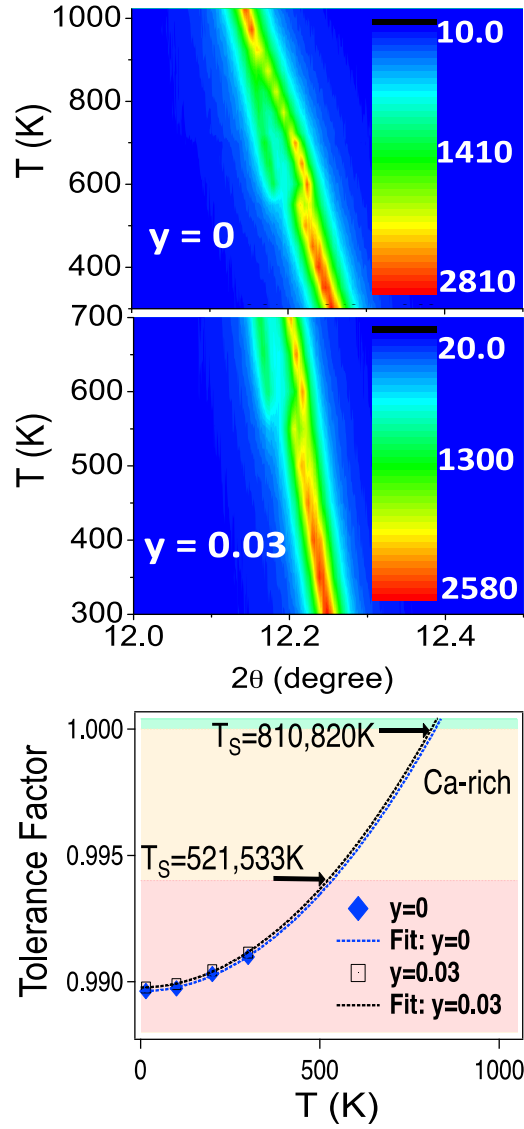
Figure 9: (Color online) Representative x-ray contour maps collected at the APS showing the structural transition temperatures for the Ca-rich samples with Nd content y of 0 and 3 %. The bottom panel displays the orthorhombic to tetragonal and tetragonal to cubic phase transition temperatures for the same samples extracted by fitting the tolerance factor curves as a function of temperature t (T) to a power law of the form t (T) = t_0(T=0K) + AT^n with n =2.
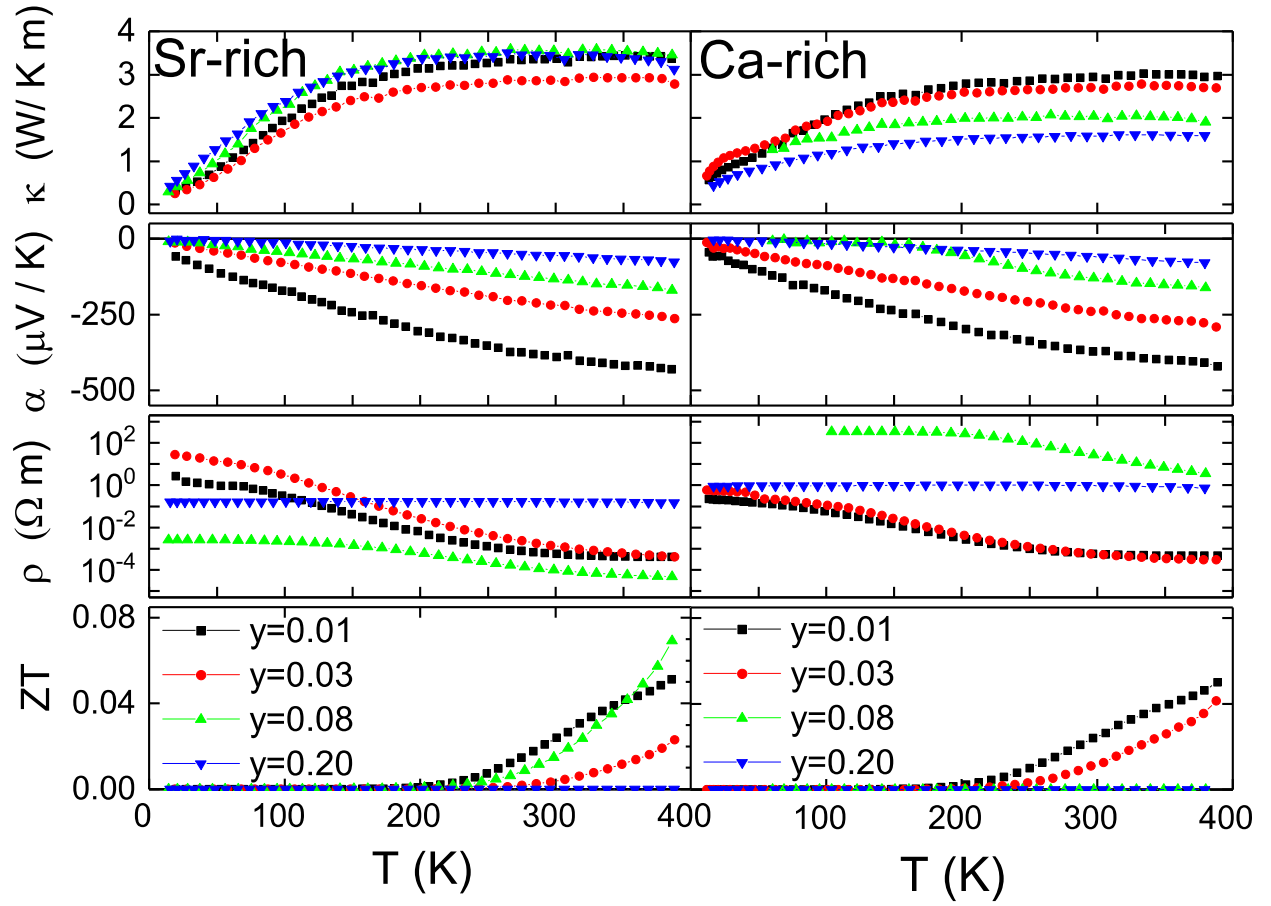
Figure 10: (Color online) (Left panel) Sr-rich thermoelectric measurements in the temperature range 13-400 K. (Right panel) Similar measurements for the Ca-rich compositions.
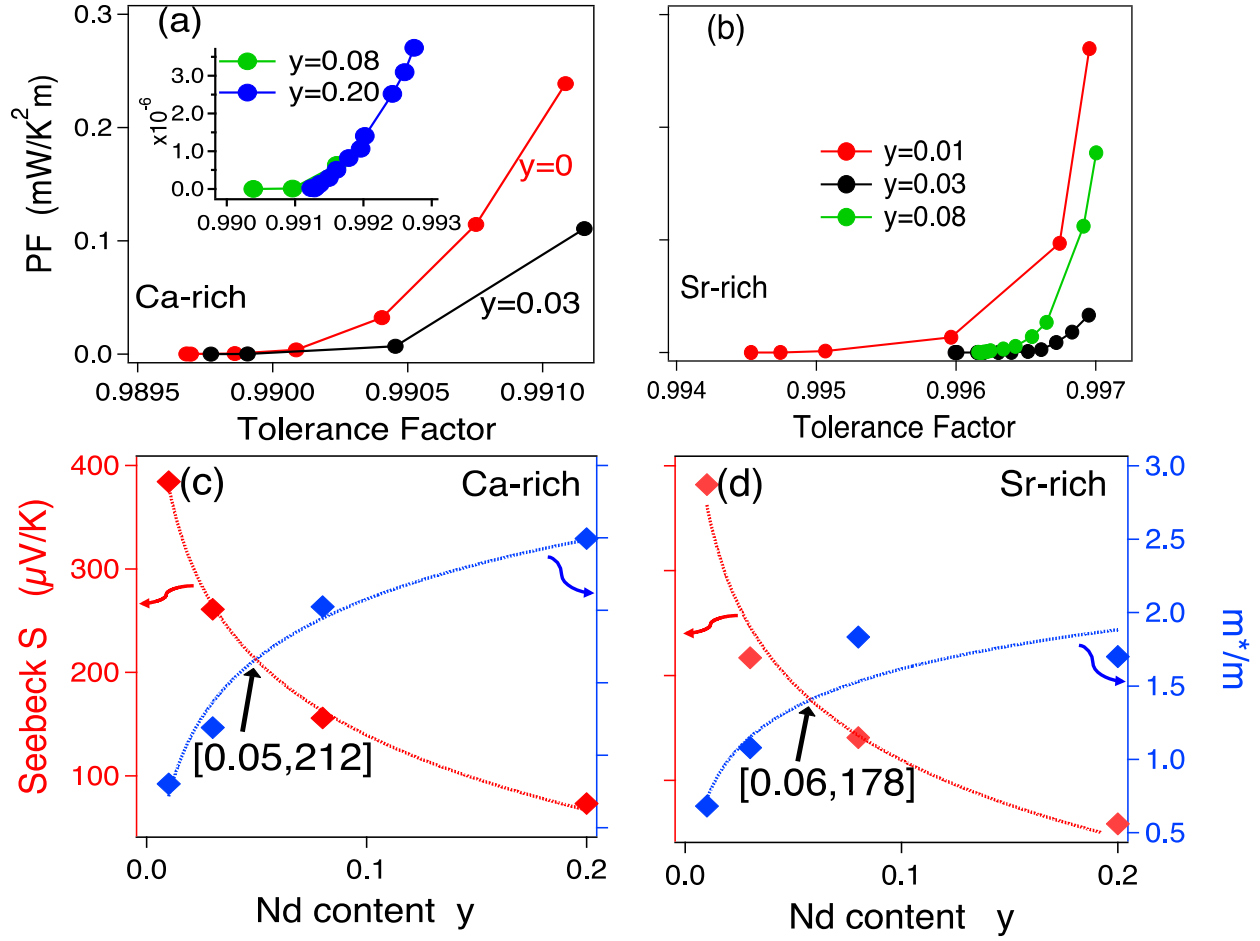
Figure 11: (Color online) (a, d) variation of the TE power factor ($S^2\,\sigma$) with the tolerance factor. Strong correlation is observed between the two parameters for all the samples. Panels (b,d) show the effect of Nd substitution (increases the electron concentration of the system) on the Seebeck coefficient S and the carrier effective mass m*. The measured negative S values indicate the nature of doping. The value of y where the two curves intersect represents the optimal Nd content $y_o \sim 0.06$ in the Sr-rich series which is quite close to the Sr-rich Nd 8% concentration observed to exhibit the best ZT value among all the compositions investigated in this work.

Table 1: Room temperature structural parameters for orthorhombic $Sr_{0.50}Ca_{0.50}TiO_3$ (SCT50) (Pbnm) obtained from neutron diffraction. Lattice parameters a = 5.47640(3) Å, b = 5.47642(3) Å and c = 7.73860(4) Å. Residual agreement factors: χ^2 =4.95 and R_{wp} =3.51%.

Atoms	x (Å)	y (Å)	z (Å)
Sr/Ca	0.9982(5)	0.0107(1)	0.25
Ti	0.5	0	0
O(1)	0.0480(1)	0.4949(2)	0.25
O(2)	0.7284(1)	0.2729(1)	0.02560(6)

Table 2: Room temperature structural parameters for tetragonal $Sr_{0.73}Ca_{0.27}TiO_3$ (SCT27) (I4/mcm) obtained by Rietveld refinement. Lattice parameters a= 5.4922(1) (Å), c= 7.7981(1) (Å). Residual agreement factors: χ^2 =4.30 and R_{wp} =3.29%.

Atoms	x	y	z
Sr/Ca	0	0.5	0.25
Ti	0	0	0
O(1)	0	0	0.25
O(2)equatorial	0.77390(5)	0.27390(5)	0

Table 3: Room temperature bond lengths extracted from our NPD refinements compared to literature values for materials of interest to this study.

Bond Type	Material	Bond Length (Å)	Structural Symmetry	Reference	T (K)
$[^{XII}Ca^{2+} - O]$	$Sr_{0.73}Ca_{0.27}$ and $Sr_{0.50}Ca_{0.50}$	2.7117(45)	I4/mcm and Pbnm	**This Study**	300
	$CaTiO_3$	2.7022(76)	Pbnm	Ref [28], NPD	296
	$Ca_{1-x}Sr_xTiO_3$ solid solution (x=0)	2.706(8)	Pbnm	Ref [55], X-ray	300
$[^{XII}Sr^{2+} - O]$	$Sr_{0.73}Ca_{0.27}$ and $Sr_{0.50}Ca_{0.50}$	2.76388(3)	I4/mcm	**This Study**	300
	$Ca_{1-x}Sr_xTiO_3$ solid solution (x=1)	2.760(1)	Pm -3 m	Ref[55], X-ray	300
$[^{XII}Nd^{3+} - O]$	Nd-doped Sr-rich series (Mean)	2.75100(9)	I4/mcm	**This Study**	300
	Nd-doped Ca-rich series (Mean)	2.7618(32)	Pbnm	**This Study**	300
	$NdTiO_3$	2.7943(3)	Pbnm	Ref[65], X-ray & NPD	290
$[^{VI}Ti^{4+} - O]$	$Sr_{0.73}Ca_{0.27}$	1.95028(9)	I4/mcm	**This Study**	300
	$Sr_{0.50}Ca_{0.50}$	1.9535(39)	Pbnm	**This Study**	300
	$CaTiO_3$	1.95083(9)	Pbnm	Ref [28], NPD	296
	$CaTiO_3$	1.956	Pbnm	Ref[7], X-ray	298
	$CaTiO_3$	1.952(6)	Pbnm	Ref[55], X-ray	300
	$SrTiO_3$	1.952(1)	cubic	Ref[55], X-ray	300
	$SrTiO_3$	1.954	cubic	Ref[7], X-ray	298
$[^{VI}Ti^{3+} - O]$	Nd-doped Sr-rich series (Mean)	1.98896(9)	I4/mcm	**This Study**	300
	Nd-doped Ca-rich series (Mean)	1.9821(1)	Pbnm	**This Study**	300
	$LaTiO_3$	2.040(3)	Pbnm	Ref[65], , X-ray & NPD	290
	$LaTiO_3$	2.0392(28)	Pbnm	Ref[66],NPD	293
	$LaTiO_3$	2.0346(5)	Pbnm	Ref[67], NPD	298
	$NdTiO_3$	2.0426(3)	Pbnm	Ref[65], , X-ray & NPD	290
	$NdTiO_3$	2.028	Pbnm	Ref[7], X-ray	298

Table 4: Transition temperatures T_S (Orthorhombic to Tetragonal to Cubic) for the $Sr_{(1-x-y)}Ca_{(x)}Nd_{(y)}TiO_3$ system with the Nd content y= 0, 0.01, 0.03, 0.08, and 0.20. The superscript c refers to extrapolated estimates from the tolerance factor curves to higher temepratures. The superscript xr refers to the APS 11BMB data represented by open circles and squares in Fig. 8 while NPD are T_S values obtained from our refinement using measured NPD data. Superscripted numbers represent literature references.

Sample	T_S(K): Orthorhombic (P*bcm*, P*bnm*, I*bmm*)→ Tetragonal (I*4/mcm*)	T_S(K): Tetragonal (I*4/mcm*) → Cubic (P*m-3m*)
$CaTiO_3$	1523 [28], 1500 [13]	1647 [28], 1618 [13],
$SrTiO_3$	-	110 [68]
$Sr_{0.50}Ca_{0.50}TiO_3$	575 [13], 536.5 ^{xr}, 533 ^{c}	923 [13], 830^{xr}, 820^c
$Sr_{0.50}Ca_{0.49}Nd_{0.01}TiO_3$	524^c	813^c
$Sr_{0.51}Ca_{0.46}Nd_{0.03}TiO_3$	519 ^{xr}, 521^c	810^c
$Sr_{0.53}Ca_{0.39}Nd_{0.08}TiO_3$	507.44 ^{xr}, 493^c	792^c
$Sr_{0.57}Ca_{0.23}Nd_{0.20}TiO_3$	410^c	746^c
$Sr_{0.73}Ca_{0.27}TiO_3$	200^{NPD}	643.1 [13], 630^c
$Sr_{0.73}Ca_{0.26}Nd_{0.01}TiO_3$	200^{NPD}	632^c
$Sr_{0.74}Ca_{0.23}Nd_{0.03}TiO_3$	125^{NPD}	631.8^c
$Sr_{0.76}Ca_{0.16}Nd_{0.08}TiO_3$	-	619.2,^{xr} 628^c
$Sr_{0.80}Nd_{0.20}TiO_3$*	250^{NPD}	550^c

* A mixed-phase sample with T_s=250K corresponding to the boundary between (I4/mcm + Ibmm) and I4/mcm.